Surface Roughness and Thermal Conductivity for Sapphire Fibers: Reducing the Thermal Noise in Gravitational Wave Interferometers

Michael A. Hall and N. John DiNardo
*Drexel University, Philadelphia, PA**

Riccardo DeSalvo
California Institute of Technology, Pasadena, CA

Takayuki Tomaru
High Energy Accelerator Research Organization (KEK), Ibaraki, Japan

Francesco Fidecaro
University of Pisa, Pisa, Italy
(Dated: May 29, 2003)

Construction of the Large-scale Cryogenic Gravitational Wave Telescope (LCGT) in Japan is expected to be completed in 2007, at which time it should become the most sensitive interferometer in operation, allowing for the possibility of observing source diffuse gravitational wave events as far away as 200 MPc. Reducing the thermal noise of the mirrors and the mirror suspension fibers is a critical part of obtaining the design sensitivity. A brief description of the mirror suspension system for LCGT will be presented and a method for improving the heat transport along the sapphire suspension fibers by polishing their surface will be evaluated. A more encompassing discussion of the relationship between thermal conductivity and surface roughness will also be presented outside the context of LCGT, including a technique to estimate the mean free path due to defects in crystals.

I. INTRODUCTION

It is postulated [1] that just as electromagnetic waves are produced as a result of an accelerating charge, gravitational waves can be produced by large accelerating masses (i.e. neutron star, black hole). As a gravitational wave propagates through space-time, it stretches space in one direction while simultaneously squeezing it in the other, alternating between the two extremes. As a gravitational wave passes through an object in space, the object will experience this stretching and squeezing effect, as shown in Figure 1.

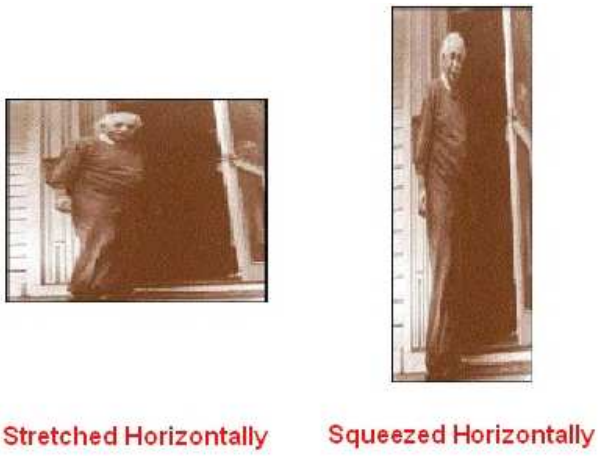

FIG. 1: Two extremes of an object's behavior as a result of a propagating gravitational wave.

In order to gain information about the particular type of gravitational wave propagating through an object, the height and width of that object needs to be measured as a function of time. The most sensitive instruments for this purpose are interferometers, based on the same principles as those used in the Michelson-Morley experiment.

Typical signals from gravitational wave events arriving at Earth are meager at best. A gravitational wave passing through an object as long as 4 km is expected to change its dimensions about one hundredth the size of an atomic nucleus, which places an extraordinary challenge at the hands of gravitational wave astronomers. Signals on this order of magnitude may be detected only after a large number of noise sources are identified and eliminated.

The expected limiting noise sources for gravitational wave interferometers are the quantum limits (radiation pressure and shot noise), the Newtonian seismic noise and the thermal noise of the mirrors and mirror suspension systems located at several points throughout the interferometer. Figure 2 shows the relative magnitude of the various noise sources encountered in the American gravitational wave endeavor, the Laser Interferometric Gravitational Wave Observatory (LIGO) project.

The quantum limits represent the ultimate sensitivity

*Electronic address: mah28@drexel.edu

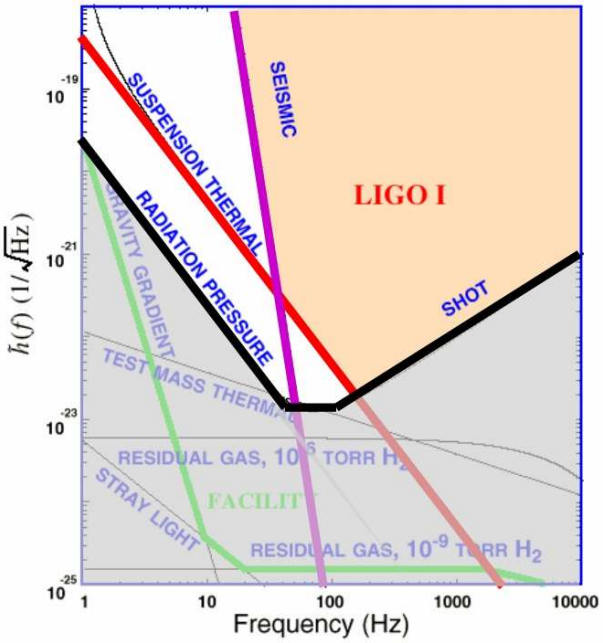

FIG. 2: Comparison of the three expected limiting noise sources in gravitational wave interferometers.

of an interferometer, which cannot be surpassed. Fortunately, many gravitational wave events are expected to produce signals well above this limit. Seismic noise, arguably the most difficult noise source to overcome, is overwhelming at low frequencies, where the majority of gravitational wave signals are expected. As a result, massive efforts are taken to push the seismic noise barrier to the lowest frequencies possible. At this point, the thermal noise of the mirror and its suspension fibers limit the sensitivity, which is expected to be one of the final barriers between the current interferometer sensitivity and that of the quantum noise limit [2].

There are three approaches to the problem of thermal noise which receive considerable attention: (1) cryogenic suspensions, and the replacement of piano wire mirror suspension fibers with (2) fused silica or (3) amorphous (glassy) metal flex joints [3]. The Large-scale Cryogenic Gravitational Wave Telescope (LCGT) in Japan has been investigating the possibility of using a cryogenic cooling system to decrease the suspension thermal noise (which is $\sim \frac{kT}{Q}$, where Q is the mechanical quality factor of the pendulum). Although this method requires a great deal of research and funding before it will become feasible, it offers a straightforward solution to the problem.

A. Mirror Suspension System for LCGT

The proposed mirror suspension setup for LCGT is shown is Figure 3. In order to reduce the thermal noise below the quantum noise limits, the temperature of the mirror must be held at 20 K. The initial cooling of the mirror does not present a significant problem. A liquid Helium thermal bath can be thermally attached towards the top of the suspension system in such a way that it does not destroy the seismic isolation. As long as the suspension system is thermally isolated from its surroundings, the mirror temperature will inevitably approach 20 K. However, under normal operation of the interferometer, 2.5 kW of laser power will be incident upon the mirror surface. A finite value for the optical absorption coefficient of the mirror will result in the conversion of laser power to heat the mirror. Therefore, to maintain a temperature of 20 K in the mirror, this heat must be transported away from the mirror as quickly as it is produced.

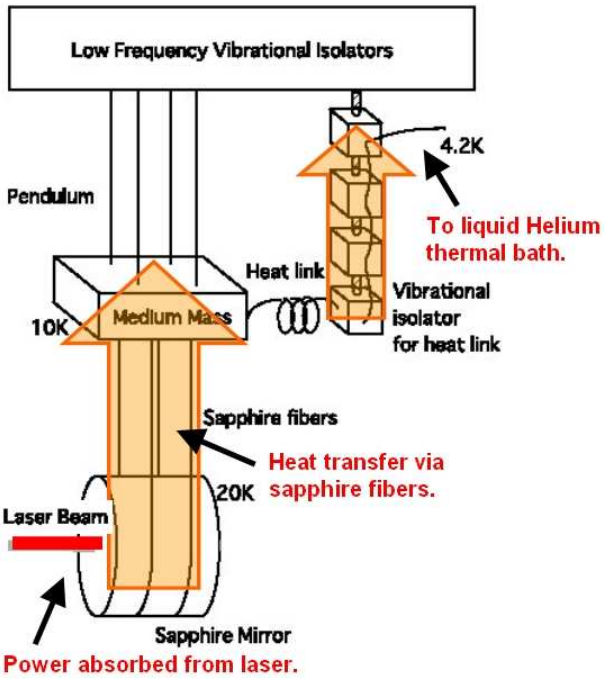

FIG. 3: Proposed mirror suspension setup for LCGT.

Tomaru et al. [4] have investigated the heat transfer along the sapphire fibers [5] used in this suspension system and have determined that it is not currently possible to maintain the design temperature for the mirror. Figure 4 shows their calculation of the maximum heat transfer versus fiber diameter for a measured value of the thermal conductivity of the sapphire fibers as obtained. The maximum heat transfer currently obtained imposes the constraint that the mirror used must have an optical absorption coefficient no greater than 2.3 ppm/cm. Unfortunately, the best available mirrors have

optical absorption coefficients of 25 ppm/cm and may be improved to 10 ppm/cm in the foreseeable future. Thus, the system must be improved by a factor ranging between five and ten.

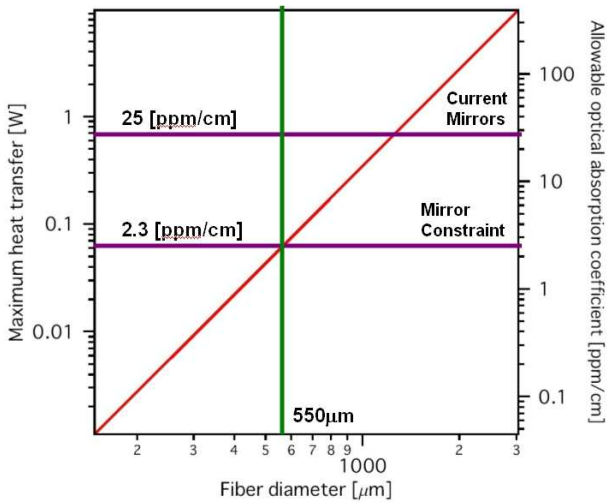

FIG. 4: Maximum heat transfer along a sapphire fiber versus fiber diameter. A particular heat transfer limits the optical absorption coefficient of the mirror if the mirror is to maintain a temperature of 20 K.

It is not feasible to make any drastic changes to the proposed suspension design because doing so could introduce extremely large increases in the seismic noise which would easily overwhelm any improvements made by reducing the thermal noise. It would also be possible to increase the thermal conductance along the sapphire fibers by making their diameters as large as needed. However, the sapphire fibers wrap around the mirror and exceeding the fiber diameter at which the minimum bending radius is equal to the radius of the mirror would cause the fibers to break. This limits the diameter of the fibers to 550 μm. In order to improve the performance of the system, the optical absorption coefficient of the mirror must be reduced, the thermal conductivity of the sapphire fibers must be improved, or a combination of both.

B. Previous Work Regarding Surface Quality

In addition to investigating the maximum heat transport along sapphire fibers, Tomaru et al. performed a simple experiment to evaluate the effect of surface scratches on sapphire fiber thermal conductivity. They obtained a standard optical sapphire fiber with a diameter of 250 μm and measured the thermal conductivity before and after scratching the surface with an #8000 diamond paste. Optical images of the surface are provided in Figure 5. It was observed that the thermal conductivity decreased by a factor of two or three in the temperature region below the thermal conductivity peak, as shown in Figure 6. Although this experiment was motivated by the desire to understand how sensitive the fiber surface is to damage during the transport of the fiber and the construction of the suspension system, it suggests that since it is possible to decrease the thermal conductivity by roughening the surface, it may be possible to improve the thermal conductivity through a series of surface treatments designed to eliminate roughness.

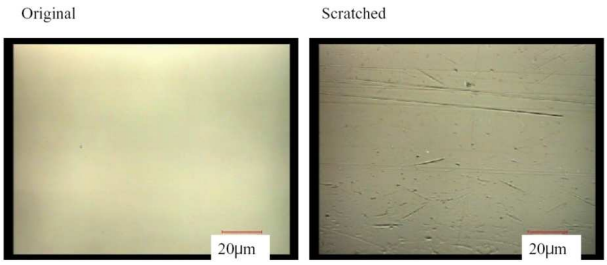

FIG. 5: Optical images of the surface of a sapphire fiber before and after scratching the surface with a #8000 diamond paste (Tomaru et al.).

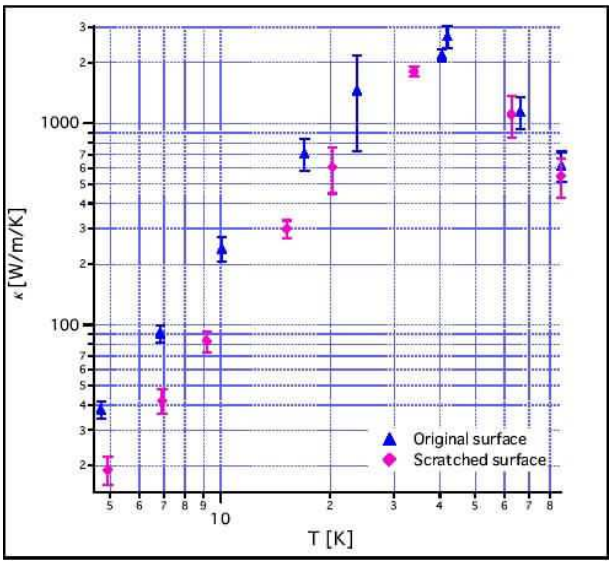

FIG. 6: Data provided by Tomaru et al. which indicates that roughening the surface of a fiber decreases the thermal conductivity below the peak.

II. DESCRIPTION OF THE EXPERIMENT

Several sapphire fibers of various diameter were obtained through the courtesy of Photran, LLC (`http://www.photran.com`). Two different kinds of fibers were used, differing only by their optimized optical wavelength

transmission. Although the optical properties are not important for this experiment, it is possible that different manufacturing processes may lead to different thermal conductivity behavior before and after roughening the surface. The properties of the fibers as obtained are shown in Tables I and II. [8]

Diameter (μm)	**Length (mm)**
420.52 ± 1.20	15.99 ± 0.06
340.03 ± 1.16	16.86 ± 0.09
$210.00 \pm \ldots$	$18.00 \pm \ldots$

TABLE I: Physical dimensions of the IR fibers.

Diameter (μm)	**Length (mm)**
$420.00 \pm \ldots$	$16.00 \pm \ldots$
$340.00 \pm \ldots$	$16.50 \pm \ldots$
$250.00 \pm \ldots$	$18.00 \pm \ldots$

TABLE II: Physical dimensions of the VIS IR fibers.

The thermal conductivity was measured over the temperature range of 2 K to 100 K using the longitudinal heat flow method, as shown in Figure 7. The sapphire fiber is fixed between a thermal bath, known as the coldfoot, and a heater. Two thermometers are located in the middle and epoxy is used to attach each device to the fiber through highly conductive copper leads. Electrical measurements of the thermistors are taken using the four probe measurement technique [9].

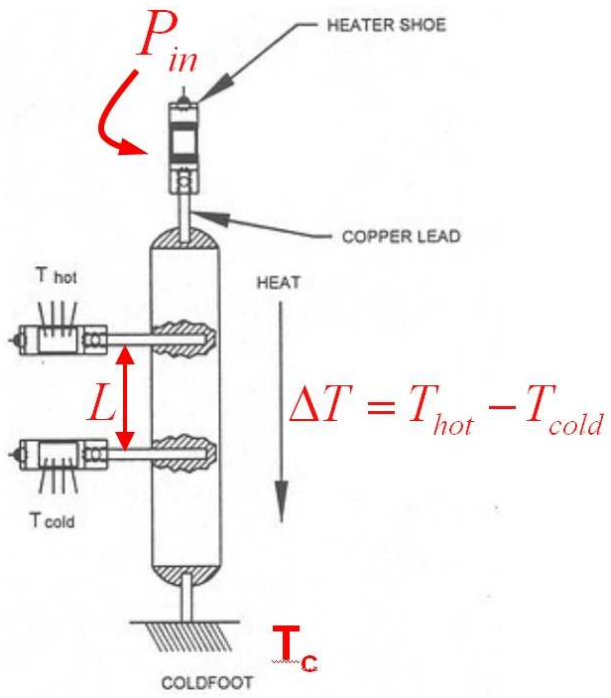

FIG. 7: Schematic of the longitudinal heat flow method.

As shown in the figure, the coldfoot is set to the temperature at which the measurement is to be taken. Next, a known power, P_{in}, is produced by the heater. After the system reaches steady-state conditions, the temperatures of the attached thermometers are recorded and their difference, ΔT, is calculated. If the length between the thermometers, L, is known as well as the cross-sectional area of the fiber, A_s, then the thermal conductivity can be calculated from the empirically established relation [10],

$$\kappa = \left(\frac{L}{A_s}\right)\frac{P_{in}}{\Delta T}, \tag{1}$$

After the sample has reached steady-state conditions, the temperatures along the sample and the power generated in the heater are measured at 25 ms intervals over a period of five minutes to obtain a reasonable error estimate.

A. Corrections

There are some small corrections which need to be considered. Not all of the heat generated in the heater flows through the sample. Some is radiated away from the sample and can be estimated by

$$P_{rad} = \epsilon\sigma_T S T^4, \tag{2}$$

where ϵ is the emissivity of the sample, σ_T is the Stefan-Boltzmann constant and S is the surface area of the heater. This correction tends to be low for temperatures less than 100 K and provides a correction of less than 1%. Some of the heat generated in the heater can flow through the electrical wires of the heater and the thermometers, which eventually provide a thermal short to the coldfoot. Although the electrical wires are thin and designed to be as thermally resistive as possible, the thermal conductance of the wires are measured directly and subtracted from the measured conductance of the sample. This can account for a correction of about 1% towards the high end of the measured temperature range. After taking these two corrections into account, the new relationship for the thermal conductivity becomes

$$\kappa = \left(\frac{L}{A_s}\right)\left[\frac{P_{in} - P_{rad}}{\Delta T} - K_{wires}\right] \tag{3}$$

The experiment is conducted at high vacuum (9×10^{-9} Torr), so the conductance due to the surrounding Helium gas is neglected.

B. Defining the Measurement Parameters

Throughout the measurement described in Section II, it is important that the temperature of the coldfoot remain constant. Failure to do so could result in large error bars in the measured temperature. It is possible to produce enough power at the heater that the temperature controller in the vicinity of the coldfoot can no longer reliably maintain its setpoint. Therefore, it is not a good idea to choose the power of the heater arbitrarily. Instead, a method for choosing the length and the magnitude of the heat pulse must be developed. It has been chosen to make the temperature difference equal to 2% of the measurement temperature. In other words,

$$\frac{\Delta T}{T} \equiv R_T = 0.02 \tag{4}$$

This signal amplitude has been chosen because it allows for a clearly visible signal that does not induce a shift in the temperature of the coldfoot.

Combining Equation (1) with Equation (4) gives an expression for the power that needs to be generated in the heater to obtain the temperature pulse desired,

$$P_{in} = R_T K T, \tag{5}$$

where the relationship that $\kappa = \left(\frac{L}{A_s}\right) K$ has been used and K is the conductance. To estimate the power to be generated in the heater, an estimate of the conductance of the sample is needed. At first, this seems to be a problem because we demand to know the conductance of the sample before measuring it. The problem is solved using an iterative process. Several measurements of the sample conductance for a 420 μm IR fiber over the temperature range of interest are made until a reasonable estimate of the conductance at all temperatures can be made. Then it is a simple matter to use this estimate and Equation (5) to obtain the power.

Under normal circumstances, a thermal conductivity measurement from 2 K to 100 K takes about two days. Due to the time constraints imposed as a result of limited access to the equipment, a process was implemented to increase the rate at which data was taken *for this iterative process only*. Instead of waiting for a steady-state for every measurement with a fixed temperature at the coldfoot, the temperature at the coldfoot is chosen to vary continuously at a steady rate of 0.1 K/s while the power generated at the heater is produced in short pulses, as shown in Figure 8.

During the heat pulse, the temperatures at the two thermometers on the sample begin to approach their steady-state values, but because the heater is turned off so quickly, fail to ever do so. It is possible to take the difference between the two temperatures and fit the data to predict the temperature difference at the steady-state using, from [9],

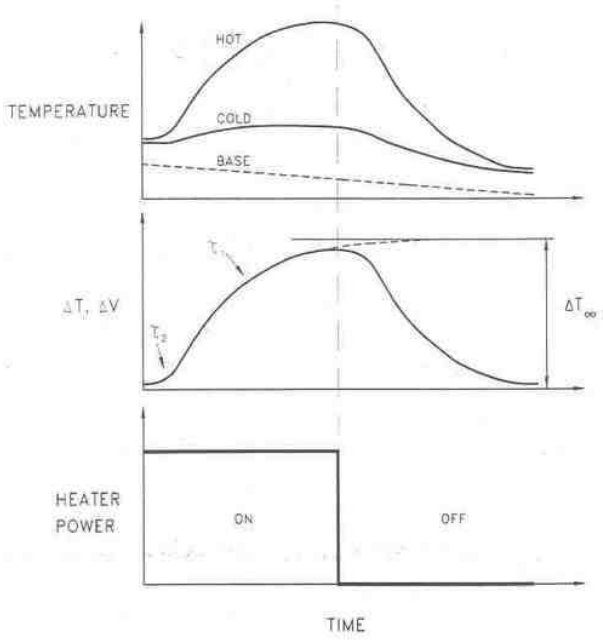

FIG. 8: Schematic of the continuous measurement.

$$\Delta T(t) = \Delta T_\infty \left[1 - \frac{\tau_1 \exp\left(\frac{-t}{\tau_1}\right) - \tau_2 \exp\left(\frac{-t}{\tau_2}\right)}{(\tau_1 - \tau_2)}\right]. \tag{6}$$

Here, ΔT_∞ is the temperature difference when the sample has reached a steady-state and τ_1 and τ_2 are long and short time constants, respectively, related to the sample and the measurement apparatus' distributed thermal capacitance and conductance.

In cases where the thermal conductivity of the sample is large, as for sapphire, the sample approaches the steady-state very quickly and the temperature difference after a short time will have come close to its value if the heater were left on indefinitely. This leads to a very good fit, which provides a reasonable estimate of ΔT at the steady-state. For samples of low thermal conductivity, however, by the time the temperature difference has grown to a significant fraction of its steady-state value, the continuously varying temperature at the coldfoot will have cycled through a wide range of temperatures, resulting in large experimental errors in the measurement temperature. Figure 9 shows the result of one such continuous measurement as just described. The plot is particularly noisy at the thermal conductivity peak because the thermal conductivity in this region changes abruptly, making it more difficult to optimize the power generated in the heater, when compared to the other, more predictable regions.

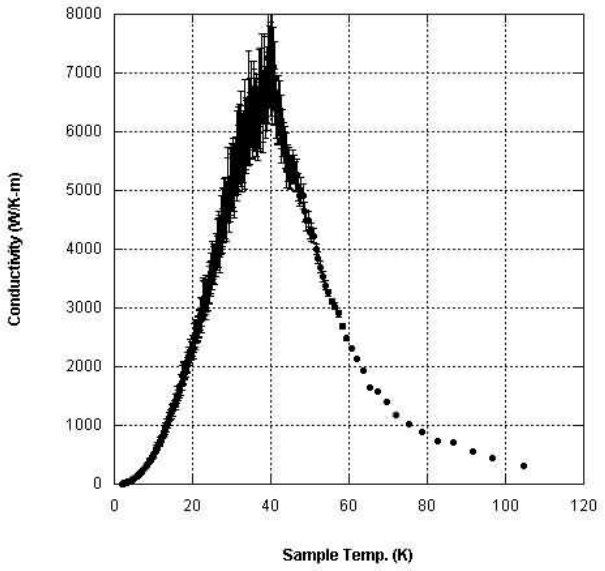

FIG. 9: Result of a particular continuous measurement for a 420 μm IR fiber.

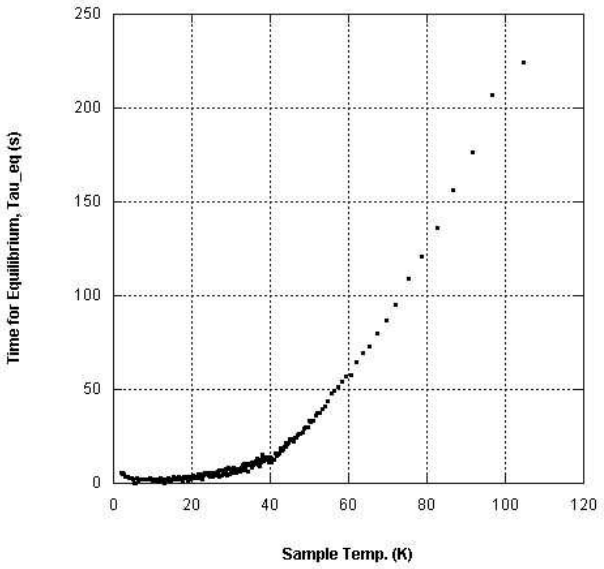

FIG. 10: Time required to reach a steady-state.

C. Preparing for a Stable Measurement

It is clear that the continuous measurement is suitable only for estimating the thermal conductivity spectrum and should not be used to collect the *real* thermal conductivity data. It is much more desirable to wait until the sample has achieved steady-state conditions before thermal conductivity measurements are made. Before the statement that the sample is in a steady-state can be made, it is necessary to define what is meant by a steady-state. For our purposes, it is sufficient to say that a steady-state exists when the temperature difference between the two thermometers attached to the sample is very close to what it would be if the heater had been left on indefinitely. The parameter τ_1 in Equation (6) is the time that it takes for the sample to reach 67% of its steady-state value. If that number is multiplied by a factor of four, the result yields the amount of time that it takes for the sample to approach 98% of its steady-state value, which we will define as the time that it takes for the sample to reach a steady-state,

$$\tau_{ss} = 4\tau_1. \tag{7}$$

A plot of the steady-state time versus temperature is shown in Figure 10.

A stable measurement is taken at various temperature intervals of the coldfoot by generating a predetermined power, from Equation (5), and waiting a predetermined time, from Equation (7). After a steady-state has been achieved, the values of the temperatures and the power generated at the heater are measured every 25 ms over an interval of 60 s in an effort to obtain reasonable error estimates and for further analysis and systematic reduction. Also, if it is determined that, for some reason, the sample did not reach a steady-state in the time provided, then the data can be fit as was the case in the continuous measurement, described in Section II B.

III. ROUGHENING THE FIBER SURFACE

A sand blasting technique was used to increase the surface roughness of each sapphire fiber as uniformly and delicately as possible, taking care not to introduce too many large scale crystal defects. An aluminum oxide abrasive powder of 15 μm sized particles was chosen because it has an identical value of Moh's hardness. The abrasive was accelerated onto the sample using a pneumatic nozzle. The properties of the fiber were remeasured after sand blasting and are shown in Tables III and IV.

To coarsely verify that the surface was roughened uniformly, optical images have been taken of each fiber under several different magnifications while passing a laser through the fiber. Original fibers that are free from surface damage will allow the laser to pass through normally, while damaged fibers will allow the laser light to leak through the surface. Figure 11 shows one such optical image which compares the laser light leaking from an original fiber to a roughened fiber. Notice that the roughened fiber appears to be emitting light uniformly, which gives the indication that its surface

Diameter (μm)	Length (mm)
413.6 ± 1.20	15.99 ± 0.06
338.5 ± 1.16	16.86 ± 0.09
$213.0 \pm \ldots$	$18.00 \pm \ldots$

TABLE III: Physical dimensions of the IR fibers after sand blasting.

Diameter (μm)	Length (mm)
$421.00 \pm \ldots$	$16.00 \pm \ldots$
$339.00 \pm \ldots$	$16.50 \pm \ldots$
N/A	N/A

TABLE IV: Physical dimensions of the VIS IR fibers after sand blasting.

is uniformly roughened. The original fibers are barely visible because most of the light is transmitted through the fiber.

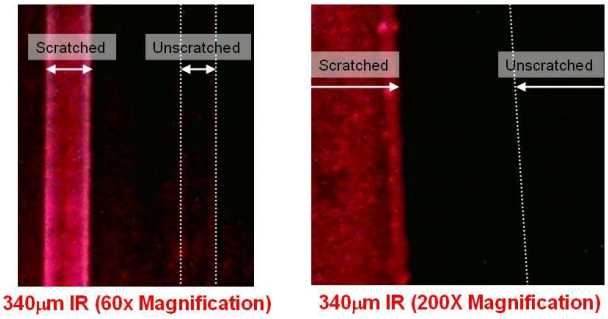

FIG. 11: Optical images comparing the laser light leaking out of a roughened optical fiber to that of an original fiber.

Although these images are somewhat convincing, more substantial evidence is desirable. Each fiber was imaged using a scanning electron microscope (SEM) before and after sand blasting. In each case, the structure of the surface was observed to have changed significantly after sand blasting as shown in Figure 12. Although these images are more convincing, it is difficult to make out the features of the surface because SEM only provides a contrast and does not offer enough insight into the height of particular surface features. This prevents us from knowing whether several of the features located in SEM images are peaks left over from etching around them or craters created from particles impacting the surface.

A third type of microscopy, atomic force microscopy (AFM), allows for the determination of height and provides a conclusive method for determining the surface structure, before and after sand blasting the fibers. AFM images obtained from the original fibers, as shown in Figure 13, indicate a relatively smooth surface. The RMS surface roughness of the surface tends to be

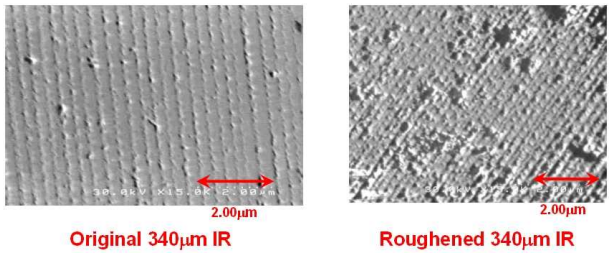

FIG. 12: Images obtained from scanning electron microscopy indicate that the surface has radically changed after sand blasting the surfaces.

about 2 nm, but this value varies slightly at different positions on the fiber surface and from one fiber to another.

AFM images obtained from sand blasted fibers reveal the existence of craters located aperiodically about the surface. These craters were not observed on the original sapphire fibers and, therefore, must be a result of the abrasive powder which was accelerated onto the surface. An AFM image for a particular fiber is shown in Figure 14. There were no noticeable differences in the surface structure between fibers optimized for IR optical transmission and fibers optimized for VIS IR optical transmission before or after roughening the surface. The RMS surface roughness after sand blasting tends to be about 4 nm, but as mentioned above, this value varies depending on fiber position and from one fiber to another.

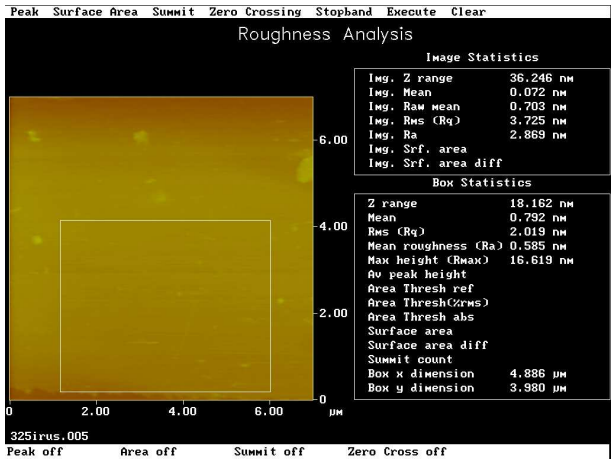

FIG. 13: An AFM image obtained from the surface of an original 340 μm IR fiber.

A. Parallel Surface Structures

Although portions of the surface are smooth, without any noticeable structure, some areas are not. In

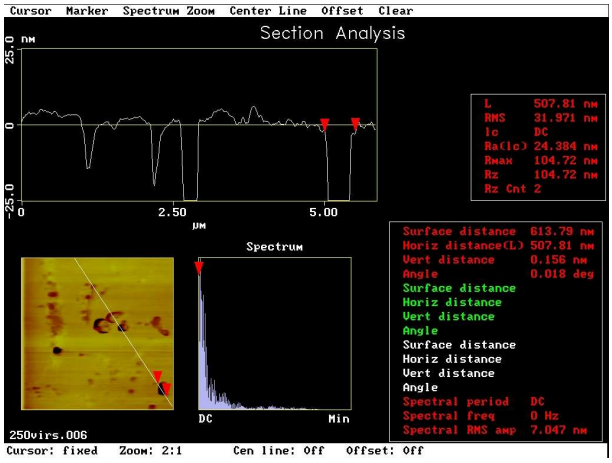

FIG. 14: An AFM image obtained from the surface of a 250 μm VIS IR fiber after sand blasting.

particular areas, parallel structures were observed to exist periodically along the axis of the cylindrical fibers, as shown in Figure 15. Although their origin is not completely understood at this time, it is likely that this is a result of the manufacturing technique.

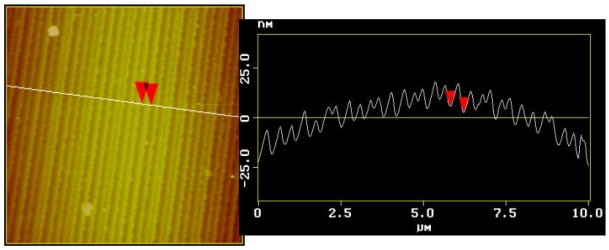

FIG. 15: An AFM image obtained from the surface of an original 420 μm IR fiber, showing the periodic structures that run parallel to the axis of the fiber.

Photran, LLC produces their fibers via the widely used Edge-defined Film-fed Growth (EFG) method. This method utilizes capillary rise from a melt source to the top surface of a die, which determines the diameter of the fiber. It is feasible that, if the die has a periodic structure due to the way that it was manufactured, these parallel structures could be an artifact of the melt solidifying as it is pulled through the die. This is still open to some debate and discussions are ongoing with representatives from Photran, LLC to confirm their source.

Whatever the source of the parallel structures on the surface of the sapphire fibers, the important question is whether or not they were roughened. Figure 16 shows that these structures were indeed damaged after sand blasting in such a way that their periodicity was destroyed. Thus, whether a portion of the fiber surface was relatively smooth or exhibited parallel surface structure, sand blasting the surface succeeded in roughening the surface in both cases.

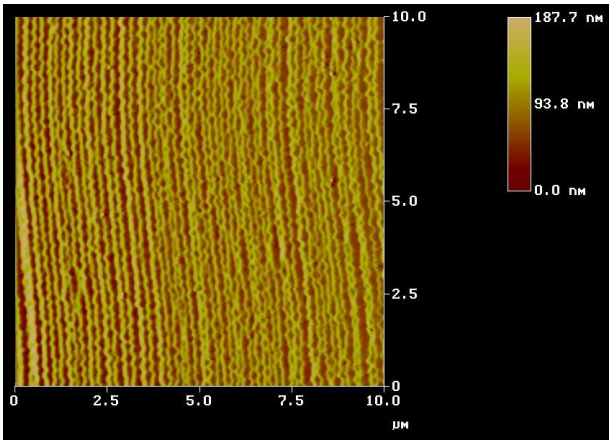

FIG. 16: An AFM image obtained from the surface of a roughened 250 μm VIS IR fiber, showing disruptions in what was previously a periodic surface structure.

IV. EXPERIMENTAL RESULTS

The experimental thermal conductivity spectra for each fiber is located in Appendix A, Figures 21 through 23. Each plot compares the thermal conductivity spectra before and after roughening the surface of each fiber. To better illustrate the experimental error in the thermal conductivity spectra, the error has been plotted as a function of temperature in Appendix B, Figures 24 through 29.

Notice that the differences are subtle and much less pronounced than the results obtained by Tomaru et al., discussed in Section I B. This may be a result of the different methods used to roughen the fibers. Before this can be confirmed, a thorough examination of the associated theory is in order.

V. THERMAL CONDUCTIVITY THEORY

The thermal conductivity of a material is equal to the thermal conductivity due to several contributions,

$$\kappa = \kappa_{phonons} + \kappa_{electrons} + \cdots . \tag{8}$$

Because sapphire is a dielectric material, the electrons are tightly bound to the nucleus so that only phonons will contribute appreciably to the thermal conductivity. This allows us to ignore all other contributions, simplifying the thermal conductivity relation. The thermal conductivity due to phonons is

$$\kappa = \frac{1}{3} C_v \overline{v} \Lambda, \tag{9}$$

where C_v is the specific heat of the material and $\overline{v}$ and Λ are, respectively, the mean velocity and the mean free path of a phonon in the material.

The specific heat is a needlessly complicated function for our purposes and it is highly desirable to do away with it, if at all possible. Because we are interested in the relative thermal conductivity between the original and roughened fibers, it is sufficient to study the behavior of the conductivity ratio. The specific heat is a property of the bulk material and is the same for both the original and the roughened fibers. Thus, taking the ratio allows for the cancellation of the specific heat and only the ratio of the mean free paths remain,

$$\frac{\kappa_1}{\kappa_2} = \frac{\Lambda_1}{\Lambda_2}. \tag{10}$$

The mean free path is determined by several different scattering processes and the three most prevalent will be considered here. When two phonons collide to create a third phonon, the wavevector of the resultant phonon is the vector sum of the wavevectors of the original two phonons. Because only phonons with a wavevector inside the first Brillouin zone are meaningful, in cases where the resultant wavevector is outside this zone, it must be brought back by adding or subtracting a reciprocal lattice vector. Thus, these processes, known as Umklapp processes, can produce a resultant phonon travelling in an opposite direction than the original two phonons. A more detailed discussion can be found in any standard solid state physics book [11]. The mean free path due to Umklapp processes (or U-proccesses), Λ_u, becomes arbitrarily large at temperatures below the thermal conductivity peak and dominates at temperatures much greater than the thermal conductivity peak.

Other important scattering processes include the mean free path due to defects or impurities, Λ_d, and the mean free path due to boundary scattering, Λ_b, which is the process whereby a phonon not only reaches the boundary of a material, but scatters in a way that changes the momentum of the phonon in the direction that is parallel to the boundary. The total mean free path of a phonon can be written in terms of the mean free paths due to the three scattering processes that are being considered, as

$$\frac{1}{\Lambda} = \frac{1}{\Lambda_u} + \frac{1}{\Lambda_d} + \frac{1}{\Lambda_b}. \tag{11}$$

Therefore, the ratio of the thermal conductivity becomes the ratio of this slightly more complicated expression for the mean free path.

A. The Polish Factor

It is possible to define the mean free path due to boundary scattering in terms of a parameter, p, known as the polish factor [12],

$$\Lambda_b = \frac{(1+p)}{(1-p)} d, \tag{12}$$

where d is the diameter of the fiber. The polish factor is defined in terms of the phonon wavelength, λ, and the RMS surface roughness of the surface, η, as

$$p(\lambda, \eta) = \exp\left(\frac{-16\pi^3\eta^2}{\lambda^2}\right). \tag{13}$$

These relationships are supported by some experimental evidence [13] and a semi-rigorous theoretical derivation [14]. For a perfectly polished surface, η approaches zero and the polish factor is equal to unity. In this case, the mean free path due to boundary scattering becomes arbitrarily large, which implies that, for a polished sample, phonons *never* scatter at the surface of a material. For surfaces that are very rough, η is large and the polish factor approaches zero. The mean free path in this case approaches the diameter of the sample, which implies that for rough samples the phonon *always* scatters at the boundary.

These two cases can be represented pictorially in Figure 17. In the case of a polished surface, phonons reflect symmetrically from the surface, maintaining a constant momentum along the direction of heat flow. It's as if the phonon never reached the surface of the material. In the case of a rough surface, the phonon can scatter in any direction, including backwards. Phonons that are scattered in this way impede the flow of heat along the fiber.

The polish factor depends on the phonon wavelength because phonons of small wavelength are more likely to scatter at the surface. This is analogous to what is already known in microscopy, whereby samples must be probed using a wavelength approximately equal to the feature size of interest. Only phonons whose wavelength is on the order of the height of the asperities (or smaller) will *see* them and be scattered isotropically.

B. The Dominant Phonon Wavelength

The polish factor is a function of phonon wavelength and, as a result, so is the thermal conductivity. Therefore, the thermal conductivity no longer represents that of the sample, but rather that of a particular phonon of

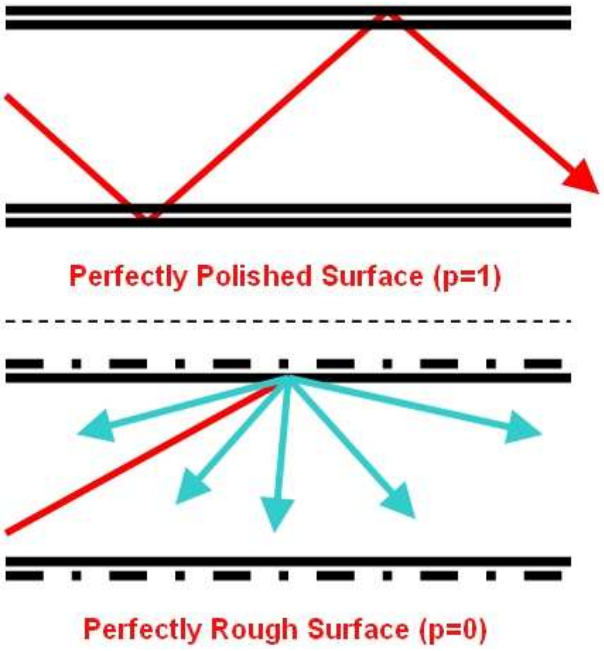

FIG. 17: Phonons reflect symmetrically from a polished surface, but scatter isotropically from a rough surface.

wavelength λ. It is not immediately obvious how to combine the contributions of several different phonon wavelengths into a single thermal conductivity of the sample. Therefore, it is convenient to make an approximation that is common throughout the literature: that all of the phonons in the material have an identical wavelength known as the dominant phonon wavelength, defined as the wavelength where the phonon distribution is at a maximum and is

$$\lambda_{dom} = 0.235\frac{h\overline{v}}{kT}, \tag{14}$$

where h and k are Planck and Boltzmann's constant, respectively. This approximation may, at first, appear to be too drastic, but it is no different than the approximation made by Albert Einstein in his theory of specific heats, where he assumed that all of the phonons in a material have an identical frequency. This simplification eliminates the wavelength dependence on the thermal conductivity ratio in favor of a temperature dependence. The final form of the thermal conductivity ratio is

$$\frac{\kappa_1}{\kappa_2} = \left(\frac{\frac{1}{\Lambda_{u_2}} + \frac{1}{\Lambda_{d_2}} + \frac{1}{d_2}\left(\frac{1-p_2}{1+p_2}\right)}{\frac{1}{\Lambda_{u_1}} + \frac{1}{\Lambda_{d_1}} + \frac{1}{d_1}\left(\frac{1-p_1}{1+p_1}\right)} \right). \tag{15}$$

C. Limiting Cases for the Thermal Conductivity Ratio

Clearly, Equation (15) could pose a significant challenge to study directly due to the number of variable parameters involved. Therefore, it is much more instructive to analyze a few limiting cases. At very large temperatures, the dominant phonon wavelength is very small because the phonons have a lot of energy. Because phonons of small wavelength are very likely to scatter from the surface, the polish factor tends towards zero. Furthermore, because of the large number of excited phonons with large energies, the occurrence of U-processes are very likely, which implies that this scattering process dominates. As a result, the mean free paths due to defects and boundary scattering are much larger than the mean free path due to U-processes and those effects can be neglected. Thus, the thermal conductivity ratio is a ratio of the mean free paths due to U-processes alone. Because the U-processes are a property of the bulk material, these mean free paths are equal and the thermal conductivity ratio,

$$\lim_{T\to large}\left(\frac{\kappa_1}{\kappa_2}\right) = 1. \tag{16}$$

As the temperature approaches zero, the dominant phonon wavelength becomes arbitrarily large and it is less likely to scatter at the boundary of the fiber. Consequently, the polish factor approaches unity and the boundary scattering terms disappear from Equation (15). At temperatures below the thermal conductivity peak, scattering as a result of U-processes become negligible and the thermal conductivity ratio is equal to the ratio of the mean free paths due to defects,

$$\lim_{T\to 0}\left(\frac{\kappa_1}{\kappa_2}\right) = \frac{\Lambda_{d_1}}{\Lambda_{d_2}}. \tag{17}$$

Now we need only to understand the behavior of the ratio between these two extremes. At some temperature significantly below the thermal conductivity peak (where defects and boundary effects begin to dominate), there exists some temperature where the dominant phonon wavelength becomes larger than the height of the asperities on the surface. At this temperature and below, some of the phonons will reflect symmetrically from the surface in addition to scattering isotropically, leading to a gradual change in thermal conductivity. Between this finite temperature and zero temperature, exists a region where the polish factor makes a transition from zero to unity and a sharp peak or valley should exist in the thermal conductivity ratio. If the RMS surface roughnesses of both fibers involved in the thermal conductivity ratio are nearly identical, then this effect should be extremely small and a small peak or valley should be present. However, as the difference between the two grow larger, the effect will become more pronounced (because the

change in thermal conductivity will occur at a different temperature for each fiber) and the peak will approach some maximum value as the difference between RMS surface roughnesses diverge.

In the temperature region above where polishing effects occur and below the thermal conductivity peak, the U-processes are negligible and the dominant phonon wavelength is small enough that the polish factor is equal to zero. In that case, the thermal conductivity ratio reduces to

$$\frac{\kappa_1}{\kappa_2} = \frac{\left(\frac{1}{\Lambda_{d_2}} + \frac{1}{d_2}\right)}{\left(\frac{1}{\Lambda_{d_1}} + \frac{1}{d_1}\right)}. \tag{18}$$

Now that we know what to expect for several different temperature regions, we can plot Equation (15) for all temperatures and identify these limits, as shown in Figure 18. For this plot, it was assumed that the mean free path due to U-processes follow a

$$\Lambda_u \propto T^{-b} \exp\left(\frac{-T}{a}\right) \tag{19}$$

behavior, where $a = 75$ and $b = 2.25$. This behavior allows for the mean free path to approach arbitrarily large values as the temperature approaches zero and to decrease exponentially at large temperatures. Values for the diameters ($d_1 = 340\mu m$; $d_2 = 250\mu m$) and the mean free path length due to defects ($\Lambda_{d_1} = 159\mu m$; $\Lambda_{d_2} = 88.1\mu m$) were chosen to represent actual parameters for the original 340 μm and 250 μm VIS IR fibers, whose experimental conductivity ratio is discussed in Section V.

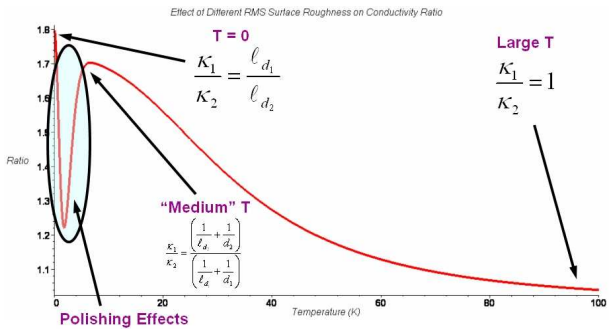

FIG. 18: The thermal conductivity ratio as a function of temperature with the various limiting cases identified.

The limits calculated in Equations (16) through (18) match up well with the indicated regions in Figure 18, as expected. The region where polishing effects are important, according to the model, occur at temperatures below that of the mirror, which would seem to indicate a problem in achieving the goals discussed in Section I A if the experimental data follows the same trend. This is discussed in detail in the next section.

VI. COMPARING THEORY TO EXPERIMENT

At first glance, the model in Figure 18 compares well with the experimental thermal conductivity ratio data for the same two fibers, shown in Figure 19 with two of the limits indicated. The model properly accounts for the thermal conductivity ratio at zero temperature and high temperatures and contains a low temperature valley and a peak at slightly higher temperatures. However, there are two problems. First, the locations of the peak and the valley in the model are shifted towards lower temperatures than in the experimental data. Secondly, the experimental data indicates that the temperature range over which polishing effects are important are spread out over a larger range than the model indicates.

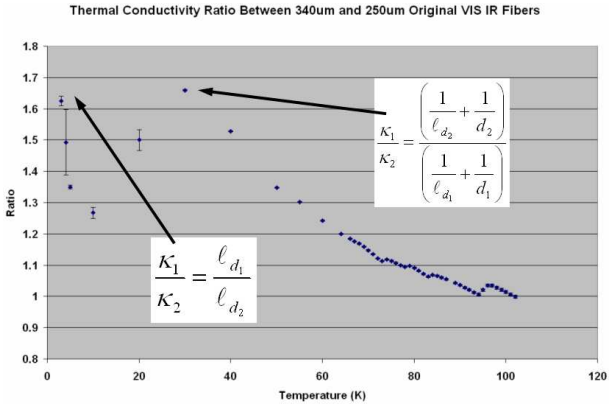

FIG. 19: The experimentally determined thermal conductivity ratio between an original 340 μm and 250 μm VIS IR fiber with two particular limiting cases identified.

The latter of these two discrepancies can be explained using a very simple argument. The model used the dominant phonon wavelength approximation, which assumes that each phonon has the same wavelength. If that were true, then as the temperature decreased from the thermal conductivity peak, eventually a temperature would be reached where the wavelength of the phonon would approach values much larger than the height of the asperities of the surface. Because all of the phonons are assumed to have the same wavelength, all of the polishing effects would happen at once as the polish factor made its transition from zero to unity. However, realistic phonon distributions are spread out over many wavelengths. Thus, decreasing the temperature would not result in affecting all of the phonon wavelengths simultaneously. First, only the longest wavelengths would be reflected symmetrically, followed by more and more if the temperature was decreased further. This is

precisely what is seen in the experimental data. This argument also explains the temperature shift in the location of the valley, a result of polishing effects.

The shift in the peak is partially explained through the same argument, but is also affected by our choice of parameters in Equation (19). Even more, if our ansatz for the form of Equation (19) is incorrect, this could significantly change the location of this peak.

A. Estimation of the Mean Free Path Due to Defects

In Section V C, three limiting cases for the thermal conductivity ratio were calculated and in Section VI it was shown that these limiting cases match the experimental data reasonably well, with minor exceptions in the polishing region and the assumed form of the mean free path due to U-processes. Equations (17) and (18) are in terms of the mean free path due to defects. The diameters have been measured and are known and the thermal conductivity ratio at any temperature has been measured experimentally. Thus, it is possible to construct two equation with two unknowns, those being the mean free paths due to crystal defects.

This is remarkable for several reasons. First, it provides a method to estimate a parameter that cannot be directly measured experimentally. Secondly, it offers a convenient way to discover whether the roughening process described in Section III has introduced any large-scale defects into the crystal. The estimated mean free paths for all fibers whose thermal conductivity ratios were clearly distinguishable are tabulated in Tables V and VI.

Fiber (μm)	Original (μm)	Roughened (μm)
420	630	573
340	1,137	***[a]
210	***	***

[a] A *** indicates that there was insufficient confidence in the location of the peaks in the thermal conductivity ratio data to determine the mean free path due to defects accurately.

TABLE V: Mean free path due to defects for IR fibers.

Fiber (μm)	Original (μm)	Roughened (μm)
420	***	***
340	159	***
250	88	N/A[b]

[b] Fiber fractured during sand blasting process.

TABLE VI: Mean free path due to defects for VIS IR fibers.

It is encouraging to note that two separate plots containing the original 420 μm IR fiber yielded nearly the same estimate for its mean free path due to defects (626 μm and 630 μm). Notice also that the only fiber that yielded an estimate of the mean free path both before and after roughening the surface (420 μm IR) shows a measurable decrease in the mean free path due to defects after undergoing the sand blasting technique. This indicates that, as gentle as we had hoped this treatment to be, it still has introduced some defects into the fiber.

VII. MAXIMUM EFFECT OF THE POLISH FACTOR FOR LCGT

At this point, it is possible to estimate the maximum increase in thermal conductivity due to polishing effects. A very rough fiber has a polish factor of zero, while a perfectly polished fiber would have a polish factor of unity. If we assume that the mean free paths due to defects are equal (such that $\Lambda_{d_1} = \Lambda_{d_2}$), then the thermal conductivity ratio for a particular fiber diameter can eventually be written in the form

$$\left(\frac{\kappa_1}{\kappa_2}\right)_{max} = 1 + \frac{\Lambda_d}{d}. \tag{20}$$

Thus, the thermal conductivity ratio increases when the mean free path due to defects is increased and when the diameter of the fiber is decreased, both of which could have been guessed beforehand, at least qualitatively. For larger diameters, phonons are less likely to reach the boundary of the material and, therefore, the surface quality of the boundary is less important. Conversely, as the mean free path due to defects is increased, than the total mean free path of the phonon becomes more dependant on the mean free path due to boundary effects at the surface. In the case of LCGT, as discussed in Section I A, the diameter of the fiber is 550 μm. In Section VI A, we estimated the mean free paths of several sapphire fibers. If these numbers are indicative of numbers that we are likely to receive for the fibers eventually used in the LCGT suspensions (which is a safe assumption), then substituting these values into Equation (20) gives a maximum thermal conductivity ratio increase somewhere between 1.2 and 3.3.

In practice, of course, it is not possible to polish the surface of a fiber with infinite precision and so it is unreasonable to presume that the polish factor of a polished fiber is *exactly* equal to unity. To the author's knowledge, the best known polishing techniques available today are offered by the Epion Corporation (`http://www.epion.com`), a JDS Uniphase company. Using their *Ultra Smoother*^{TM} *Processing System*, based on gas cluster ion beam (GCIB) technology, they claim to be able to achieve an RMS surface roughness on the Angtstrom level, as demonstrated in an AFM image of

a Tantalum sample in Figure 20. This technology is typically used on silicon wafers, but has been successful on most flat surfaces and it is not yet certain whether this would work just as well with fibers. However, if it is possible to polish the surface to an RMS surface roughness of 4 $\mathring{A}$, from an original RMS surface roughness of 2 nm, this corresponds to a thermal conductivity increase of approximately 1.8 in the vicinity of 10 K to 20 K. If LCGT is to reduce the thermal noise below the quantum noise limits, this still requires the optical absorption coefficient of the mirror to be reduced by a factor of six.

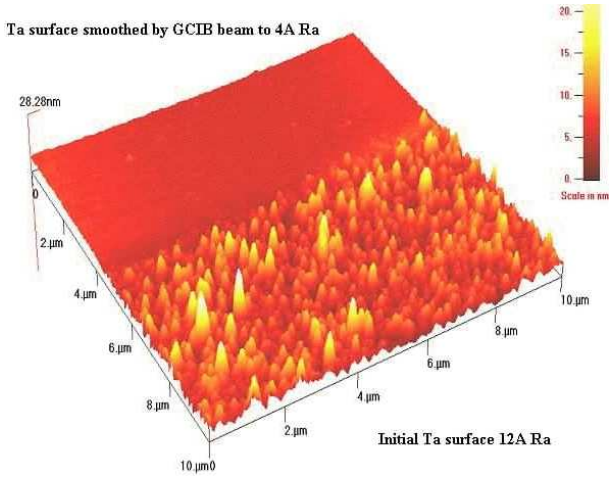

FIG. 20: Tantalum surface before and after application of Epion's GCIB polishing technique.

VIII. CONCLUSIONS

A consistent model of the thermal conductivity ratio between two different sapphire fibers was introduced by considering the scattering effects as a result of U-processes, defects and impurities, and the boundaries of a material for a cylindrical fiber. This model describes the thermal conductivity behavior of a sapphire fiber both before and after roughening the surface to a large extent and provides an explanation for experimental data. Furthermore, it reveals a way to estimate the mean free path due to defects, a quantity that cannot be measured directly through experimental techniques.

An expression for the maximum thermal conductivity increase due to polishing effects was obtained for a fiber of diameter d. Although under ideal surface conditions, this expression indicates that the thermal conductivity of the sapphire fibers proposed for use in the LCGT mirror suspension system may be increased by as much as a factor of 3.3, depending on the number of defects in the crystal, realistic expectations for the surface quality may limit this number to 1.8. Even if the best polishing techniques available today for silicon wafers can be used for sapphire fibers, this would still require the optical absorption coefficient of the mirror to be improved by a factor of six.

If sand blasting the surface introduced measurable amounts of crystal defects, then the methods employed by Tomaru et al. probably introduced even more. It is likely that their previous observation that the thermal conductivity decreased by a factor of two or three at temperatures below the thermal conductivity peak was primarily induced by the introduction of large-scale defects into the crystal, which would have easily masked any polishing effects. This argument is strengthened further by the observation that polishing effects dominate at temperatures below 20 K, which implies that any difference in the thermal conductivity spectra above 20 K and the temperature at which the thermal conductivity peak occurs could not have been a result of polishing effects. Indeed, even the model presented in Section V B qualitatively (and to a limited extent, quantitatively) indicates this type of behavior.

IX. FUTURE WORK

From the standpoint of LCGT, the most useful prospect for future work is undoubtedly polishing a group of sapphire fibers (possibly through the application of GCIB techniques provided by Epion, Inc.) to see if their thermal conductivity can be increased, as expected. Regardless of how small an effect it may be, even a factor of two increase below a temperature of 20 K would relieve some of the pressure to produce a mirror with an improved optical absorption coefficient.

It would be interesting to repeat the experiment performed by Tomaru et al. as closely as possible, this time taking far more data points, and use the methods developed in Sections V C and VI to verify whether the effects that were observed were due primarily to a decrease in the mean free path due to defects or polishing effects.

It would be useful to improve the model described by Equation (15) by introducing a more realistic phonon distribution, because it is likely that this would broaden the temperature range that is affected by polishing effects as indicated by the experimental data.

Lastly, it is important to fully understand the parallel surface structures shown in Figures 15 and 16. Dialogue between the author and representatives from Photran, LLC will continue in an effort to determine if they are, as is currently suspected, an artifact of the manufacturing process.

X. ACKNOWLEDGEMENTS

Larry Rothrock from Photran, LLC for donating the several sapphire fibers used during this experiment.

Hareem Tariq for her assistance during the sand-blasting process.

Charles Bordier for his assistance during the sand-blasting process as well as in using the scanning electron microscope to obtain images of the fibers before and after scratching their surface.

Xavier De Lépine for his assistance in defining a high quality thermal conductivity measurement using the Quantum Design PPMS. His work regarding the verification of accurate power readings and the investigation into the time constant of glassy metal samples at differently temperatures was particularly useful.

APPENDIX A: EXPERIMENTAL THERMAL CONDUCTIVITY SPECTRA

Figures 21 through 23 compare the thermal conductivity spectra between the original fibers to the same fibers after sand blasting their surface. There is no comparison for the 250 μm VIS IR fiber, because this fiber was broken during the sand blasting process. As a result, only the thermal conductivity for the original fiber is shown on the right of Figure 23.

APPENDIX B: EXPERIMENTAL ERROR IN THE THERMAL CONDUCTIVITY SPECTRA

To better illustrate the experimental error in the thermal conductivity spectra, Figures 24 through 29 show the error as a function of temperature. The larger error that consistently appears in the temperature range where the thermal conductivity peak occurs (about 35 K) indicates that perhaps there are some sources of systematic error which have not been completely accounted for. However, these errors are still well within acceptable limits and should not seriously undermine any of the results discussed earlier.

APPENDIX C: EXPERIMENTALLY OBTAINED THERMAL CONDUCTIVITY RATIO PLOTS

Figures 30 through 32 show the experimentally determined thermal conductivity ratio plots for several combinations of sapphire fibers which are currently understood. The large number of data points for each thermal conductivity spectrum allowed for the possibility to accurately interpolate between them. Values obtained using interpolation methods assured that a good estimate of the thermal conductivity could be made for all temperatures, allowing the ratio to be taken at predetermined values of the temperature. The structure of these plots are discussed in detail in Sections V C and VI. Notice that the plots in Figure 32 have a slightly different structure than the others. The rise in ratio as the temperature goes to zero indicates, from Equation (17), that the mean free path due to defects has decreased by about a factor of two in each case. It may be a result of improper handling of the fibers at some point after the original thermal conductivity measurement or may suggest that the amount of defects added to a sapphire fiber during the sand blasting process is a function of its exposure time.

[1] P. Saulson, *Fundamentals of Interferometric Gravitational Wave Detectors*, p. 9, World Scientific (1994).

[2] B. Barish, *Workshop on Astrophysical Sources for Ground-Based Gravitational Wave Detectors*, Drexel University (October 30, 2000).

[3] R. DeSalvo, *Low-Frequency GW Interferometric Detectors*, Gravitational Wave Advanced Detector Workshop, Elba, Italy (May 24, 2002).

[4] T. Tomaru et al., Phys. Rev. Lett. A **301** (2002) 215.

[5] Mono-crystalline sapphire fibers are being used as the suspension fibers because of their high thermal conductivity [6] and mechanical quality factor [7] at cryogenic temperatures.

[6] Thermophysical Properties of Matter, Vol. 2, Thermal Conductivity-Nonmetallic Solids, The TPRC Data Series, IFI/PLENUM New York-Washington (1970).

[7] T. Uchiyama et al., Phys. Lett. A **273** (2000) 310.

[8] Some errors are not yet available.

[9] Quantum Design, *PPMS Thermal Option User's Manual*, (`http://www.qdusa.com`)

[10] A rigorous solution to the three-dimensional heat equation yields the same result for an insulated cylindrical rod with a fixed temperature at one end and a point heat source at the other.

[11] C. Kittel, *Introduction to Solid State Physics: Seventh Edition*, p. 133, John Wiley & Sons (1996).

[12] H. B. G. Casimir, Physica **5** (1938) 495.

[13] R. Berman et al., Proc. Roy. Soc. A **231** (1955) 130.

[14] J. M. Ziman, *Electrons and Phonons*, p. 456, Oxford University Press (1979).

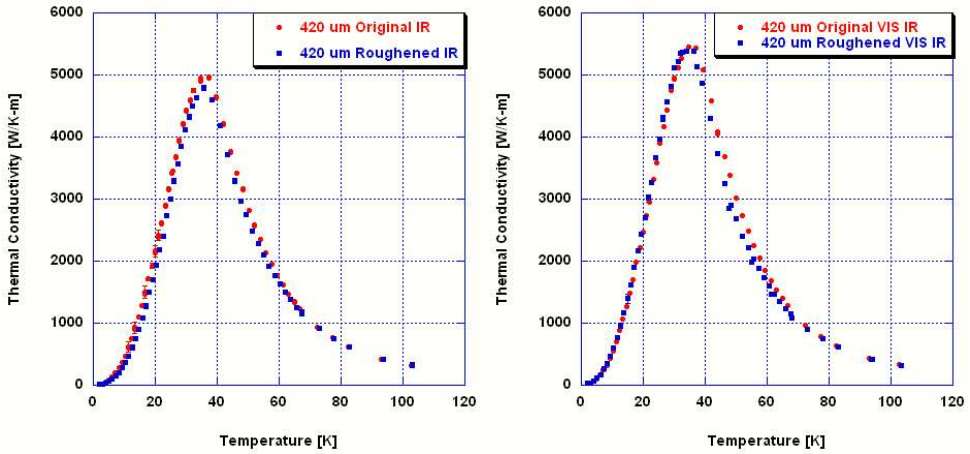

FIG. 21: Thermal conductivity spectra comparison for the 420 μm IR (left) and VIS IR (right) fibers.

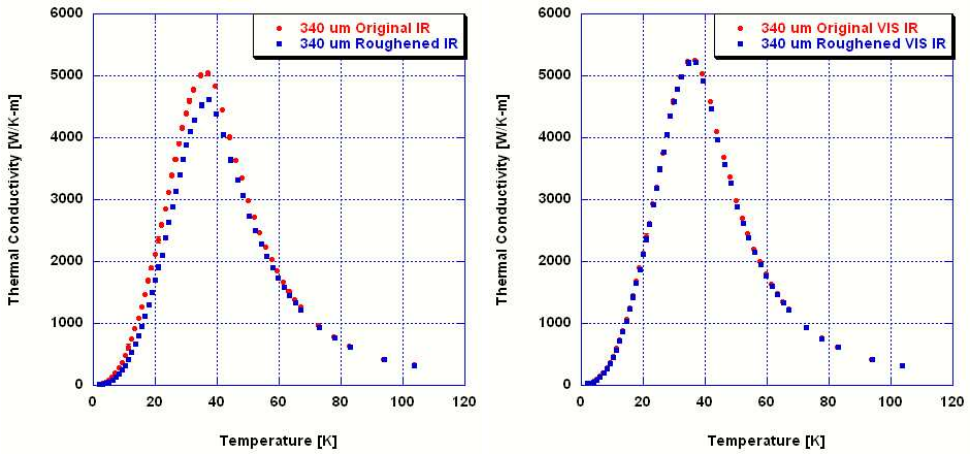

FIG. 22: Thermal conductivity spectra comparison for the 340 μm IR (left) and VIS IR (right) fibers.

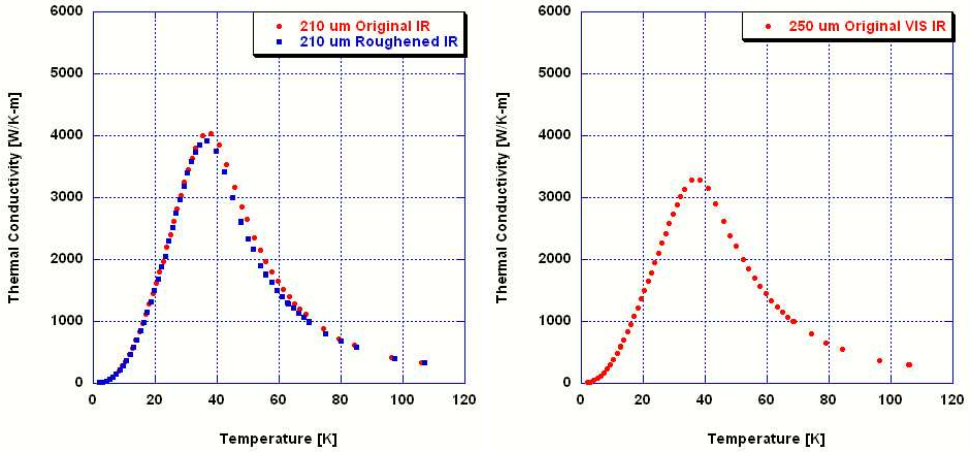

FIG. 23: Thermal conductivity spectra comparison for the 210 μm IR (left) and the 250 μm VIS IR (right) fiber.

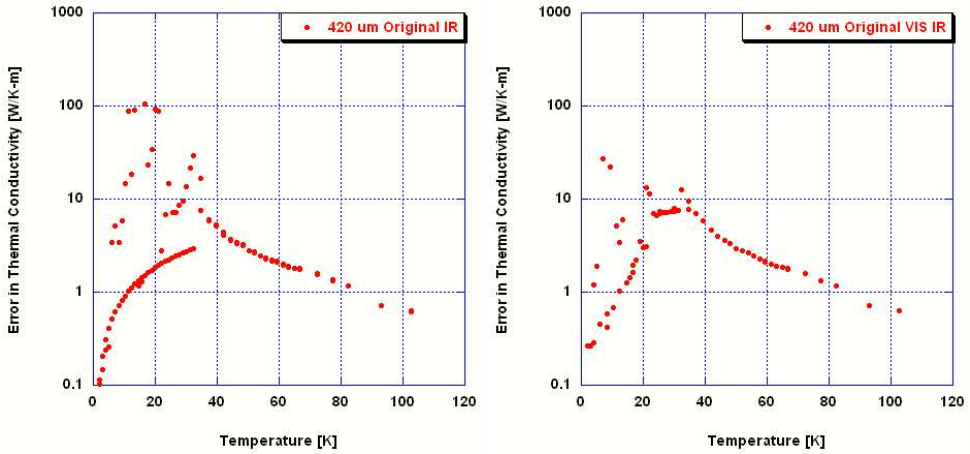

FIG. 24: Experimental error in the thermal conductivity for the original 420 μm IR (left) and VIS IR (right) fibers.

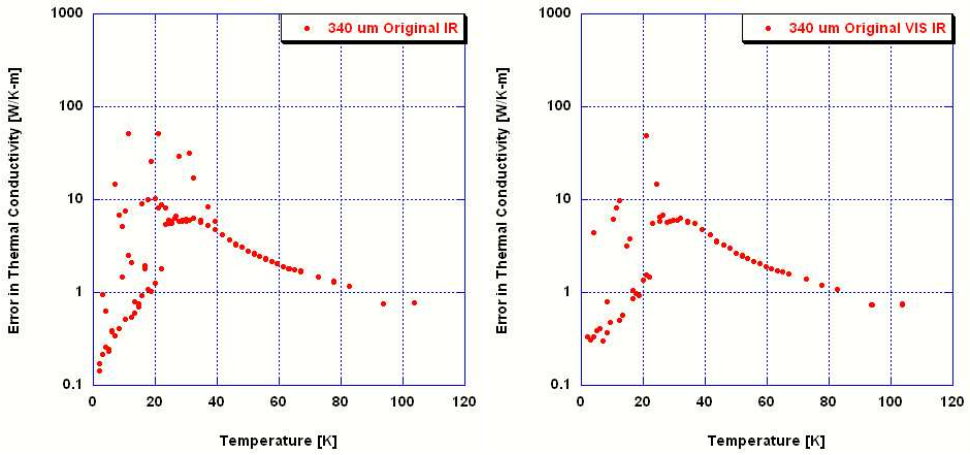

FIG. 25: Experimental error in the thermal conductivity for the original 340 μm IR (left) and VIS IR (right) fibers.

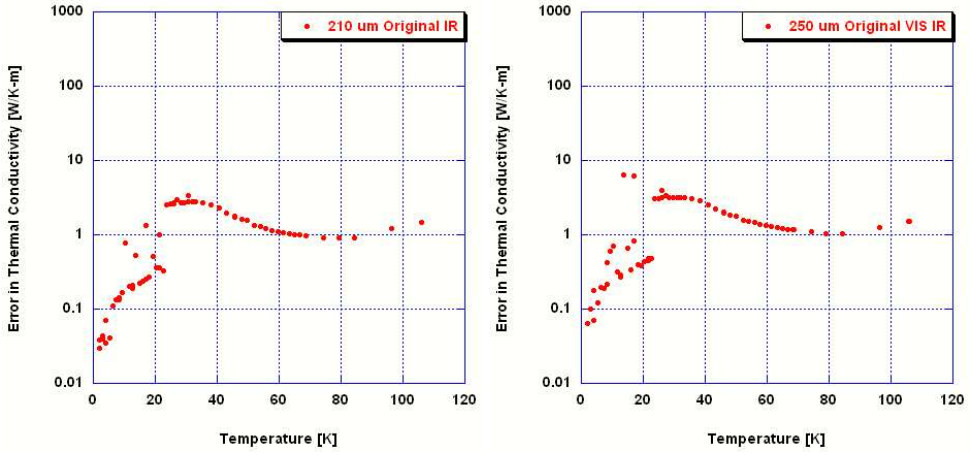

FIG. 26: Experimental error in the thermal conductivity for the original 210 μm IR (left) and VIS IR (right) fibers.

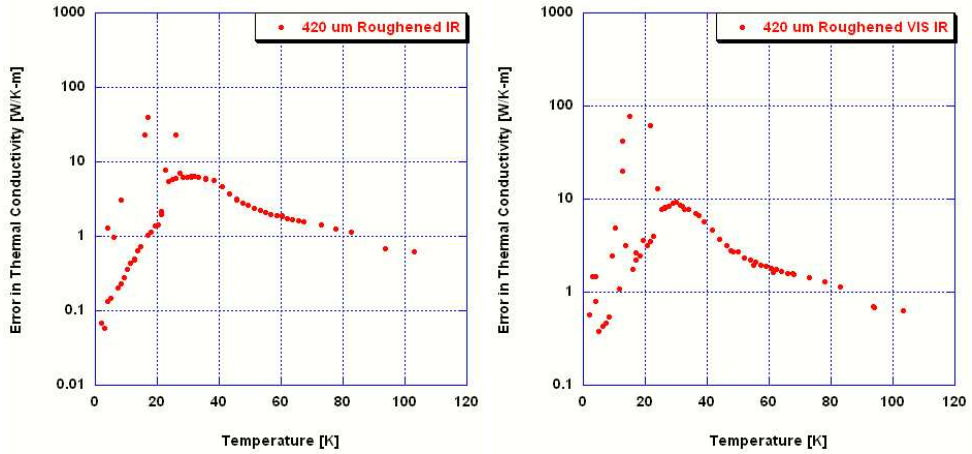

FIG. 27: Experimental error in the thermal conductivity for the roughened 420 μm IR (left) and VIS IR (right) fibers.

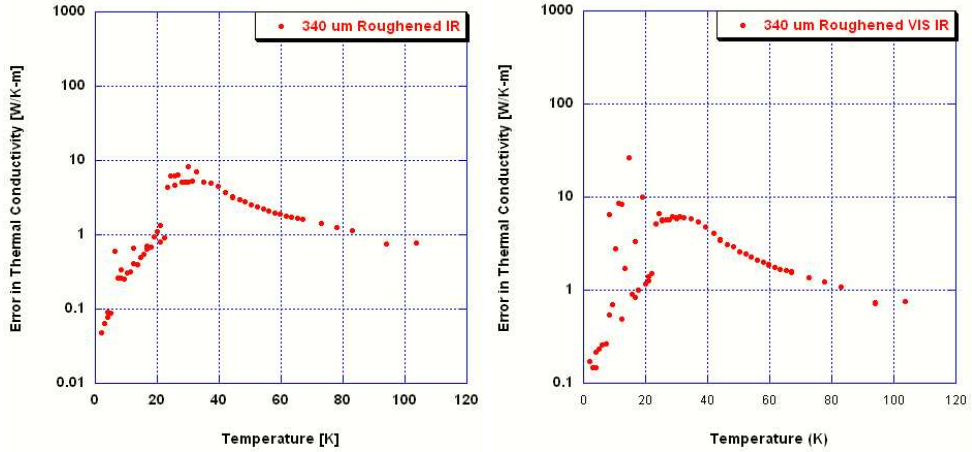

FIG. 28: Experimental error in the thermal conductivity for the roughened 340 μm IR (left) and VIS IR (right) fibers.

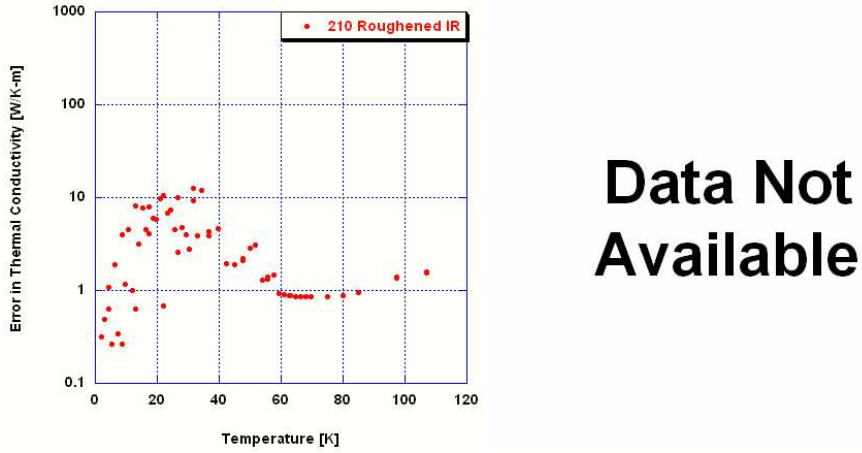

FIG. 29: Experimental error in the thermal conductivity for the roughened 250 μm IR (left) and VIS IR (right) fibers.

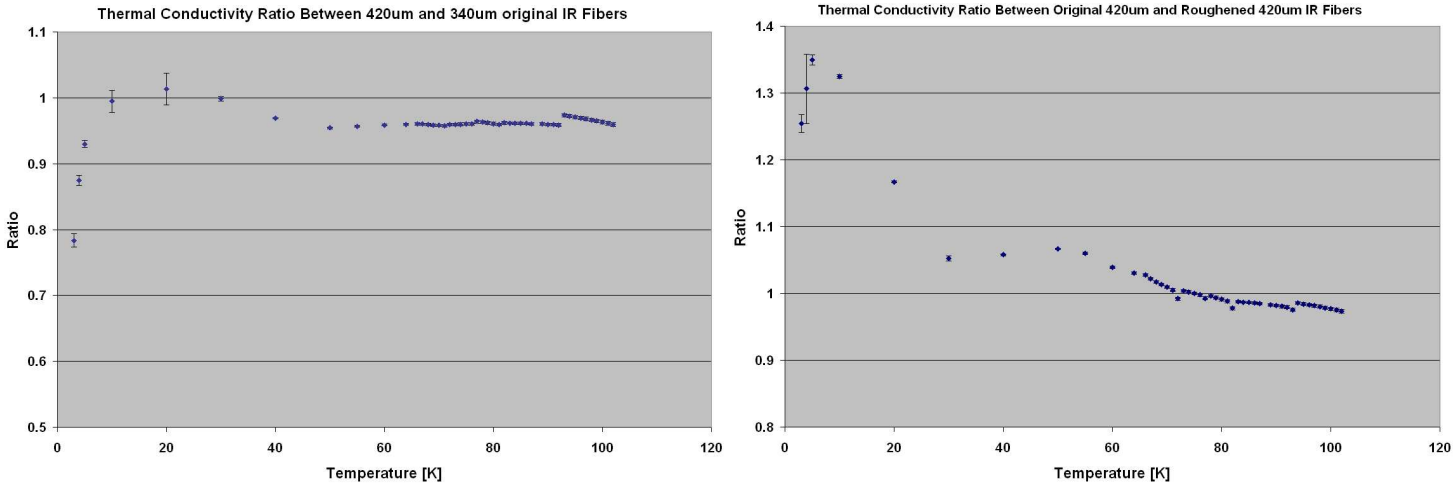

FIG. 30: Experimentally determined thermal conductivity ratios for two pairs of IR fibers. The plot on the right is the ratio between an original and a roughened 420 μm IR fiber.

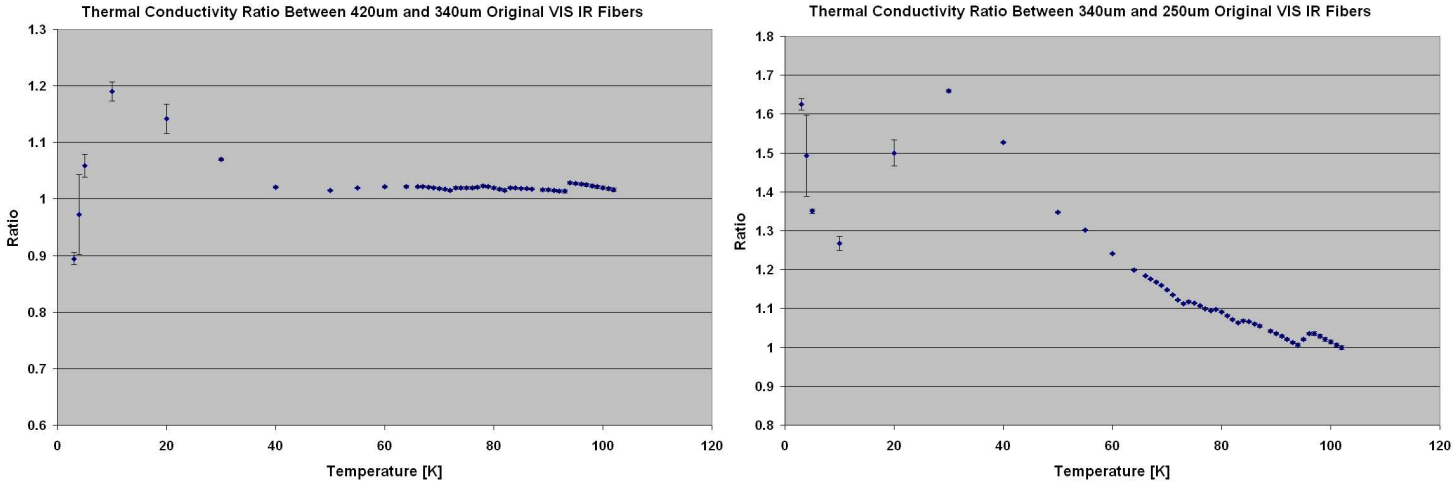

FIG. 31: Experimentally determined thermal conductivity ratios for two pairs of VIS IR fibers.

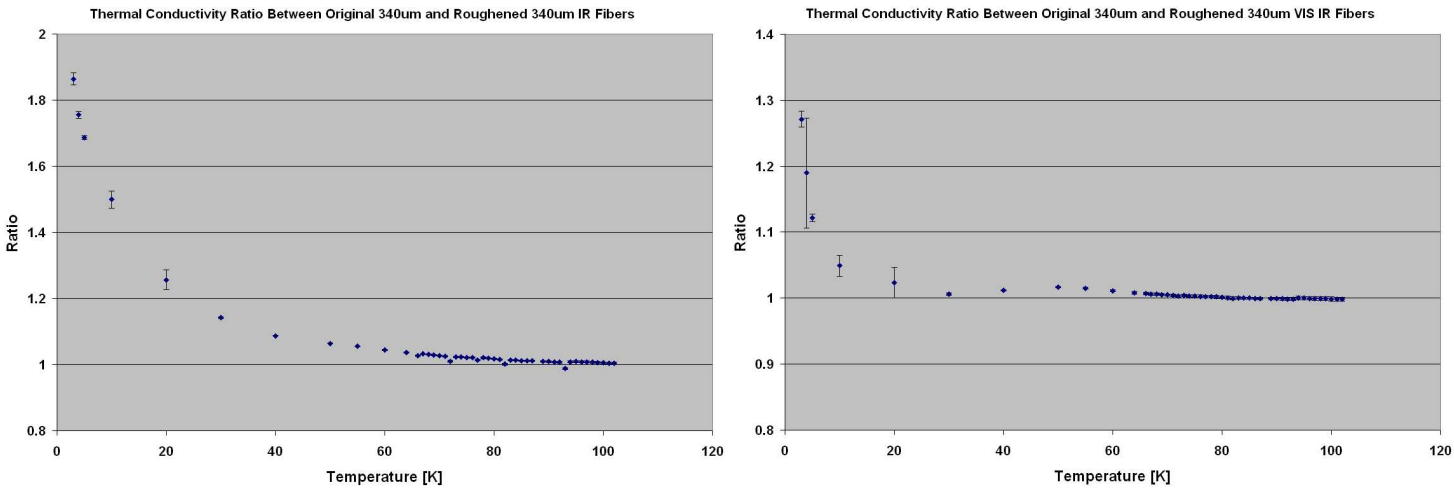

FIG. 32: Experimentally determined thermal conductivity ratios for two pairs of fibers that appear to have suffered a significant increase in the number of crystal defects as a result of the sand blasting process.